Mechanism and Machine Theory 160 (2021) 104264

Contents lists available at ScienceDirect

Mechanism and Machine Theory

journal homepage: www.elsevier.com/locate/mechmachtheory

Research paper

Experimental measurement and finite element simulation of elastic-body vibration in planetary gears

Tristan M. Ericson[a,1], Robert G. Parker[b,2]

[a] Department of Civil and Mechanical Engineering, York College of Pennsylvania, York, PA 17403, United States
[b] Department of Mechanical Engineering, University of Utah, Salt Lake City, UT 84112, United States

ARTICLE INFO

Article history:
Received 14 December 2020
Revised 20 January 2021
Accepted 20 January 2021
Available online 23 February 2021

Keywords:
Planetary gear
Mode shape
Elastic deformation
Ring vibration
Mesh deformation
Gear experiments

ABSTRACT

Modal vibration experiments and finite element modeling reveal elastic-body continuum vibration in planetary gear components at frequencies within operating speeds. Sixteen equally-spaced accelerometers measure elastic-body vibration of the ring gear in ten vibration modes. Several of these modes were predicted – with good frequency accuracy – by a lumped-parameter model because their elastic-body vibration is moderate but not dominant compared to discrete-body vibrations. Other modes dominated by elastic-body vibration were missed entirely by the model. One mode has dominant planet elastic-body vibration. Experiments showing elastic-body vibration are compared to an established finite element/contact mechanics model with good agreement. Additionally, experimentally measured ring gear nodal diameter components agree with analytical model predictions in the literature. Elastic-body vibration persists for the same system configured with three, four, and five planets. Each mode has significant tooth mesh deformation, so dynamic mesh excitation sources are likely to strongly excite them. The test planetary gear, which is closely based on a conventional helicopter planetary gear, is not intentionally designed to highlight elastic vibration behavior, so elastic-body modes are likely active in numerous practical systems.

1. Introduction

Planetary gears are manufactured with increasingly lighter and thinner components to reduce weight and introduce compliance into the system, especially in high-speed applications. Design optimization and tight tolerances have allowed these traditionally heavy components to shed significant weight, and the lighter, thinner components are more elastically deformable. Gear designers usually desire some form of system compliance to compensate for manufacturing errors and help with load sharing [1–3]. The added compliance from thinner gears is useful in that regard. Lightweight gears, however, present modeling and design challenges. Gears with significant elastic-body vibration are not well described by lumped-parameter models that focus exclusively on discrete-body motion of the gears as lumped masses. Elastic-body modes are prominent in new applications of elastic rings operating at high speed [4]. Additionally, elastic-body deformation disrupts load distribution [5] and introduces new failure modes with high stress concentrations in gear bodies promoting crack propagation and fatigue [6], which has been identified as the primary cause of failure in helicopter components [7].

E-mail addresses: tericson@ycp.edu (T.M. Ericson), rob.parker@utah.edu (R.G. Parker).
[1] Associate Professor
[2] Professor

https://doi.org/10.1016/j.mechmachtheory.2021.104264
0094-114X/

Basic lumped-parameter planetary gear models restrict analysis to rotational motion of each gear, see Hammami et al. [8], though most literature sources include translational degrees of freedom resulting from finite bearing and support structure stiffness. August and Kasuba [9] consider translations of the sun gear only. Other researchers include translational motions of all gear bodies to develop a more complete rotational/translational in-plane model [10–16]. Kahraman [17] compares the modes given by a purely torsional model to a transverse-torsional model given in [11]. Additionally, there are full three-dimensional models that include all rotational and translational motions of each gear body [18–20]. These lumped-parameter models, however, are unable to capture any elastic-body vibration of system components.

The ring gear is most susceptible to elastic deformation, and planetary gear models considering elasticity focus on this component first. The literature covers elastic vibration of rotating rings with the inextensible assumption thoroughly [21–24]. Elastic-body deformation of ring gears in planetary systems has been studied by finite element analysis and analytical models. Kahraman and Vijayakar [25], Kahraman et al. [26], and Ge and Zhang [27] use entirely finite element based approaches, focusing particularly on ring gear deformation. Abousleiman and Velex [28] and Abousleiman et al. [29] use a hybrid finite element/lumped-parameter model to include elasticity of the ring gear (with 12 degree of freedom beam elements) and carrier (with a finite element mesh). This modeling approach was later used to optimize tooth profile modifications [30]. Zhang et al. [31] also discretize the ring gear to incorporate its flexibility into a lumped-parameter model. Wei et al. [32] present a new hybrid model using virtual equivalent shafting elements to balance modeling accuracy (poor in many lumped-parameter models) with complexity (high in finite element models). Zhang et al. [33] further use this model with ring gear, carrier, and shaft elasticity to study natural frequencies and vibration modes. Zeng et al. [34] present a space-time model that combines lumped-parameter analysis with finite element analysis to predict the vibration spectrum of an operating wind turbine. Zhang et al. [35] used a hybrid model to study the effect of planetary gear journal bearing errors on load sharing performance.

Analytical methods of modeling ring gears, according to Tanna and Lim [36], compare well against finite element models that include tooth and spline geometries for the radial inextensible modes. Wu and Parker [37–39] use a fully analytical approach to model the ring gear as an elastic continuum to study planetary modal properties. Wang and Parker [40] present an expanded analytical model that considers high-speed effects, and the results are compared to a finite element/contact mechanics model. Wang et al. [41] also use an analytical approach to study ring gear mode shapes. Chen et al. study ring gear deformation by modeling this component as a uniformly curved Timoshenko beam to analyze the effect of ring gear thickness and support type (fixed or pinned) [42], as well as number of supports [43], on mesh stiffness and natural frequency. They further use this modeling approach to include ring gear flexibility into fault analysis [44].

There is, however, little published experimental data that examines the dynamic elastic-body deformation of planetary components. Hidaka et al. conducted several planetary gear experiments and published a series of papers. In their second report [45], they see that elastic continuum deformation dominates ring gear displacement in experiments. In their third report [46] they use finite element modeling to further explore ring gear deformation. The ring gear is distorted into a triangular form (in the shape of a three nodal diameter mode [47]), which was also observed by Oda and Miyachika [48], but the deformation is caused by mean (not fluctuating) planet-ring tooth loads from the spatial periodicity of the three planet gears and does not appear to reflect dynamic vibration of the ring gear because the deformed shape rotates with the carrier. In their seventh report [49], Hidaka et al. studied the effect of ring gear thickness on stress and load distribution. They find that ring gear compliance is not necessary when the sun gear is floating, and the ring-planet mesh may not engage properly with an elastically deformed ring gear, elevating stresses at the tooth tip if the ring gear is too thin. Similarly, in more recent experiments Kahraman et al. [50] show that a flexible ring gear improves load sharing only slightly in systems with a floating sun gear. In other cases, however, they demonstrate that ring gear flexibility and support conditions significantly affect planet loads and tooth stresses. Vicuña and Chaari [51] compared experimental measurements to numerical analysis, but their measurements were limited to a single accelerometer on the exterior of the ring gear. Mbarek et al. [52] compared a lumped-parameter model to experiments on a back to back setup with more comprehensive instrumentation, similar to our previous work in [53]. They mounted accelerometers to the ring gear, sun gear, carrier, and planet pins to conduct modal testing and spinning test experiments, but like our prior research, focused on discrete-body motion. There are no thorough experiments demonstrating elastic-body vibration in planetary gears compared to an established modleing technique in the literature.

Lumped-parameter analytical models capture vibration modes characterized by non-deformable (rigid) gear bodies connected by a network of stiffnesses representing the gear meshes, bearings, and other compliant elements. These are called “discrete-body” vibration modes in this paper. Discrete-body modes observed in prior experiments related to the current paper were separated into two categories in [53]: low frequency “fixture modes” and high frequency “gear modes.” Fixture modes are dominated by compliance in the sun gear/carrier shafts and support bearings. The planetary gear components (i.e. sun, planets, ring, and carrier) move according to nominal gear kinematics with little dynamic tooth mesh strain in fixture modes. In contrast, gear modes are characterized by significant tooth mesh and planet bearing strain energy. Gear modes show notable relative motion between planetary gear bodies and generate greater tooth and planet bearing forces, which gives them greater practical importance than fixture modes. Discrete-body modes exhibit lumped-parameter rotational and translational vibrations where the only compliance is from the discrete mesh, bearing, and support stiffnesses. Lumped-parameter models do not capture elastic vibration of the gear bodies. We refer to modes having enough continuously-deformable elastic vibration to prevent accurate or complete description by lumped-parameter modeling as “elastic-body” modes, in contrast to “discrete-body” modes. Elastic-body modes are the focus of this paper.

Our work considers elastic-body vibration modes discovered in experiments and finite element/contact mechanics modeling. We present experimentally measured elastic-body vibration in the ring gear and, surprisingly, the planet gears. This dynamic behavior was not originally a research target. Previous work focused on comparing experimental measurements of discrete-body modes with lumped-parameter and finite element models [53] and improving the effectiveness of simulation tools [54], focusing on discrete-body motion. During those experiments, however, additional resonance peaks not captured by the lumped-parameter model were measured by sensors used in the test setup. Analysis in this paper shows that this phenomenon is caused by elastic-body vibration in the ring gear and/or planet gears. After further evaluation, we now regard most or all of the gear modes previously assumed to be entirely discrete-body in nature to be "moderately" elastic-body modes, although lumped-parameter modeling predicts their natural frequencies with good accuracy. There are additional previously undiscovered modes with "dominant" elastic-body characteristics. Measured elastic-body vibration is verified by a finite element/contact mechanics model, and ring gear nodal diameter components observed in experiments match analytical model predictions. The elastic-body modes have large tooth mesh deflection and experience significant dynamic mesh loads in operation. The experimental planetary gear has practical dimensions similar to a long-used production helicopter gear whose ring gear is relatively thick compared to many modern ones and has relatively stiff supports. The frequencies of vibration modes considered in this paper are within the operating mesh frequency range of helicopter gears and other practical systems.

2. Experiments

Fig. 1 depicts the experimental test stand. The custom fixtures, test articles, and setup are discussed in detail in [53]. A spur planetary gear similar to a production helicopter one is stationary during testing. The ring gear mates to the fixtures with a slip fit and is secured by 16 bolts. A static torque is applied to the carrier while the sun and ring gears are rotationally constrained by the fixtures, thus loading all the tooth meshes. An MB Dynamics Modal 50 shaker excites the system near one planet-ring mesh. A network of uniaxial accelerometers measures the dynamic behavior of the system. Four accelerometers are mounted tangentially to the sun gear, carrier, and planet gears near meshing interfaces. The ring gear has 16 equally spaced accelerometers oriented radially. Fig. 1 shows that a load cell at the end of a radial arm (A) mounted to the bedplate

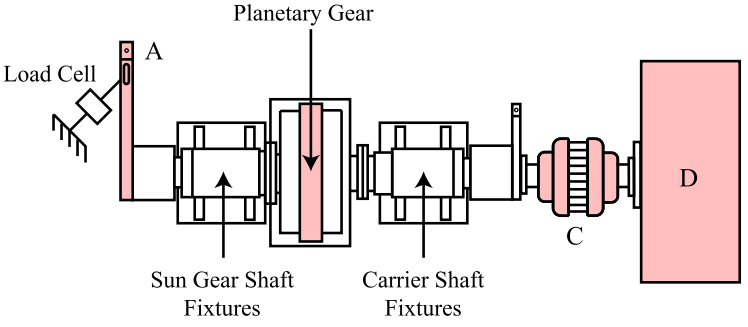

Fig. 1. Planetary gear modal testing setup top view schematic diagram showing (A) a load cell arm that fixes the input shaft to the bedplate through a load cell and (C) a compliant coupling that isolates the gearbox from (D) the torque actuator.

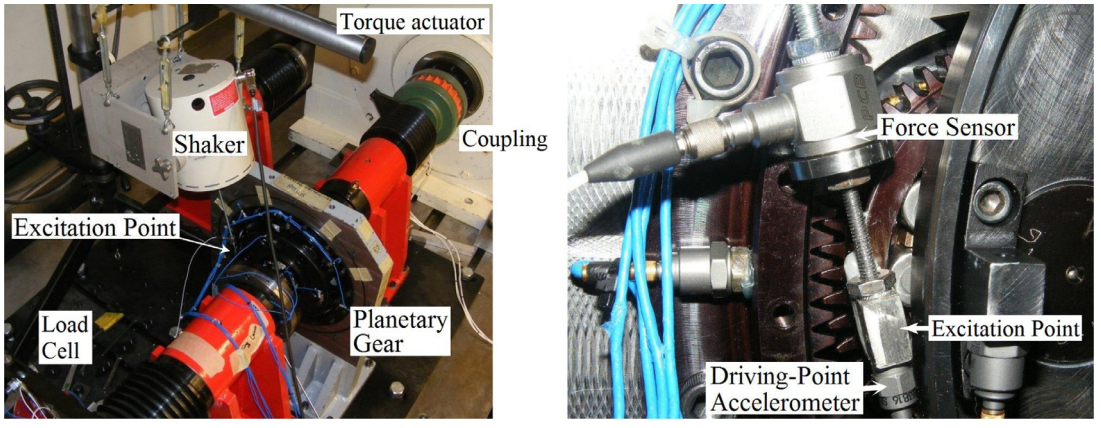

Fig. 2. Planetary gear modal testing setup photographs showing (a) the spur planetary gear excited by the modal shaker and (b) the shaker stinger attached to planet gear one parallel to the ring-planet line of action with a force sensor and a driving point accelerometer.

Table 1
Basic dimensions of the experimental custom planetary gear.

	Sun gear	Planet gears (3–5)	Ring gear
Number of teeth	65	55	175
Module [mm]	1.609	1.609	1.609
Tooth thickness [mm]	2.00	2.00	2.00
Facewidth [mm]	10.0	8.00	10.0
Pressure angle [deg]	15.97	15.97	
Center distance [mm]	96.52		
	Diameters [mm]		
Base	100.6	85.08	270.7
Root	97.91	81.78	288.0
Tip	107.8	91.69	278.9

fixes sun gear shaft rotation and measures the applied preload torque. A compliant coupling (C) connects the system to the torque actuator (D), which acts as a rigid boundary. Fig. 2 shows photographs of the experimental system from overhead with the modal shaker stinger attached directly to a planet gear with a force sensor to measure the input excitation and a driving point accelerometer. The shaker stinger is attached along the line of action of the planet-ring gear mesh. This modal shaker testing setup allows excitation and measurement up to high frequencies and convenient sensor placement without the safety concerns and complexity associated with spinning tests. Speed limitations of the fixtures and drive components in spinning tests are also not an issue with the modal testing setup. Dimensions of the test stand, specifications of the data acquisition system, and procedures for modal shaker excitation and data processing not specific to elastic-body vibration analysis are contained in [53].

Elastic-body motion, as described throughout this paper, was initially identified with the 16 bolts that mount the ring gear to its fixture torqued in place. Once this phenomenon was identified, however, data was collected with the bolts "snugged" in place to permit a little more elastic-body deformation. This improves data quality by ensuring that measured vibration is within sensor capability and above the noise floor. The difference between torqued bolt data and snugged bolt data is noticeable but not extreme because the slip fit with the fixtures provides additional restraint. Results presented later derive from snugged ring gear bolt experiments.

The planetary gear used in the experiments is a custom gear design. Table 1 gives the basic parameters. Systems with three, four, and five equally-spaced planets were tested. The mass and stiffness parameters are given in [53] for what is called "Gear B" in that paper. The gear modes in that work were contained in the 1400–3450 Hz range with the fixture modes in a lower frequency range. Although the gearset in question is a custom design for experimentation, its dimensions, masses, and stiffnesses are similar to those of a production helicopter planetary gear, referred to as Gear A in [53], that had a 1850–2900 Hz gear mode range. We are less concerned about the lower frequency fixture modes because they are largely dominated by parameters of the supporting fixtures and contain minimal strain energy in the gear meshes and planet bearings.

All experimental results in this paper are acquired by shaker testing with excitation on the planet gear body parallel to the line of action with the ring gear, as depicted in Fig. 2. Except when noted otherwise, experiments are conducted on the three planet configuration with 102 N-m applied torque at the sun gear.

2.1. Instrumentation

Sensor placement extends from previous experiments designed to capture discrete-body motion. Tangentially-mounted uniaxial accelerometers have been positioned to measure rotational and translational vibration of the carrier, sun gear, and two of the planet gears since the discrete-body mode research. Five of the same type of accelerometers were mounted radially around half the circumference of the ring gear with an expectation that the ring gear would not vibrate much, given its stiff support structure. This accelerometer configuration could detect discrete-body motion and/or indicate the presence of elastic-body motion. Once elastic-body deformation was discovered, additional radial ring gear accelerometers were added to measure all the way around the ring gear and to increase the spatial measurement resolution. Fig. 3 shows the 16 radially-mounted ring gear accelerometers that are suitable for capturing elastic-body vibration. Additional accelerometers for measuring elastic-body deformation could not be easily added to other gear bodies and the existing instrumentation on the carrier, sun gear, and planet gears from prior experiments is not oriented to measure radial elastic-body deformation. For example, Fig. 4(a) shows that two planet gears have tangentially-mounted accelerometers attached via an accelerometer adapter flange in Fig. 4(b) bolted rigidly to each planet gear. This sensor orientation is not conducive to studying the motion of interest now, and sensor orientation is not easily changed considering the tight fixture tolerances.

Fig. 3 shows that the ring gear accelerometers are mounted to capture only radial elastic-body vibration, not tangential. The literature and our experiments show that this accelerometer configuration is sufficient to capture general motion of the ring gear provided the ring is approximately inextensible [55]. Hidaka [45] and Botman [56] claim that ring gear motion is primarily characterized by radial elastic-body deformation. Nevertheless, to test this assumption, accelerometers were

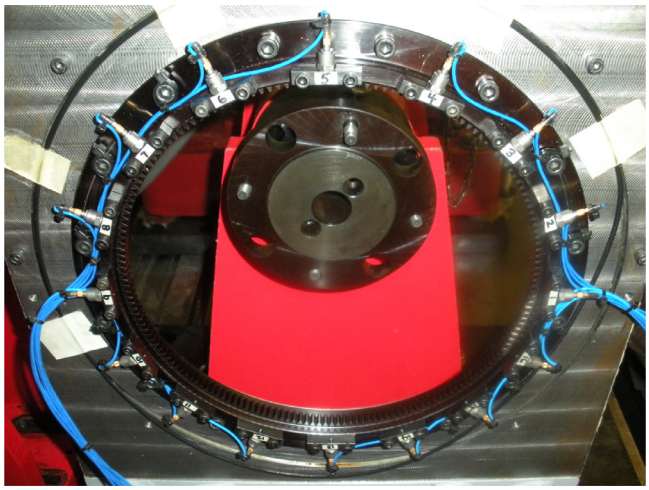

Fig. 3. Radial accelerometers mounted directly to the ring gear.

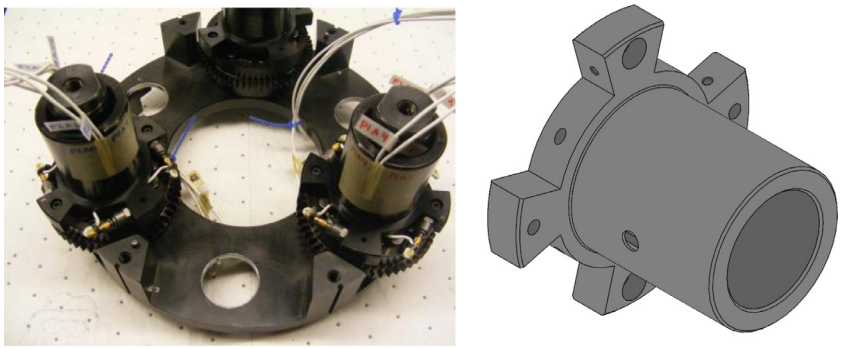

Fig. 4. Tangential accelerometers attached (a) to planet gears through (b) rigidly mounted adapter flanges.

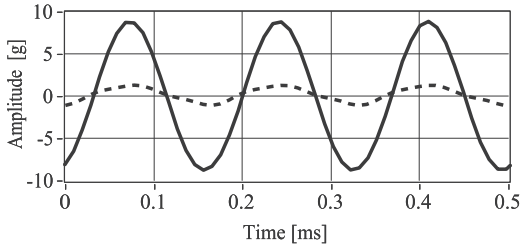

Fig. 5. Steady state radial (solid) and tangential (dashed) vibration of the ring gear at the 3 o'clock position (accelerometer #1 location) aligning with the x_t-axis in Fig. 6. Shaker excitation is on a planet gear body parallel to the line of action with the ring gear. The applied torque is 339 N-m at the sun gear. The excitation frequency is 6000 Hz.

positioned radially and tangentially on the ring gear. Fig. 5 shows the vibration response of these two components in steady state at 6000 Hz. The radial component is an order of magnitude larger than the tangential component. Consequently, our subsequent measurements consider only the radial vibration component.

Fig. 6 notes ring gear accelerometer numbers and highlights key locations used to identify elastic-body vibration in experiments. More than one accelerometer location is needed to identify all elastic-body modes because certain ones may have a node of zero vibration amplitude near any given accelerometer. The accelerometer numbers used coincide with node locations in the finite element/contact mechanics model (e.g. accelerometer #5 in experiments and node #5 in the finite element/contact mechanics model are both in the twelve o'clock position on the ring gear).

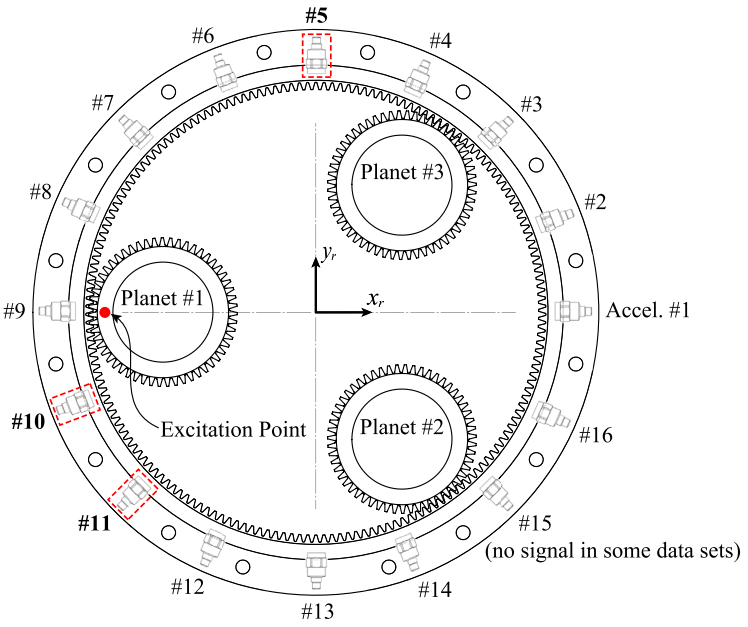

Fig. 6. Ring gear accelerometer configuration in experiments (coinciding with elastic node locations in the finite element/contact mechanics model). The key accelerometers #5, 10, and 11 used in frequency response plots are highlighted.

2.2. Experimental data processing

Natural frequencies are experimentally identified in frequency response graphs. This data was acquired by shaker testing with incremental steps through the frequency range of interest. At each frequency the system was excited by the shaker at steady state to obtain the response of all components or points of interest. Each data point in these plots represents the results of one block of data collected in this manner.

Experimental vibration shapes are a snapshot in time of the experimental data at the instance of maximum deflection for a given excitation frequency. For sinusoidal response where acceleration is proportional to displacement ($\ddot{x}(t) = -\omega^2 x(t)$),the measured acceleration amplitudes can be used to generate the experimental vibration shape diagrams presented throughout the paper. This produces a reliable depiction of the mode shape when modes are well-spaced and lightly damped. We believe that this is reasonably true for most modes considered in this paper, but accurate characterization of some modes will inevitably be contaminated, to some degree, by nearby modes. For this reason we often use the term *vibration shape* to describe the actual experimentally measured motion of the planetary gear at a natural frequency. The vibration shape is equivalent to the mode shape when no nearby modes meaningfully influence the measured behavior and the system is lightly damped.

Vibration shapes contain a mix of discrete-body and elastic-body characterization. Discrete-body translational motion of a gear body is illustrated by the position of a solid red circular body shifted away from its nominal position, which is indicated by a dotted black line. The mass center trajectory of planet discrete-body translational motion is given by a (usually ovular) solid black line. The discrete-body rotation is indicated by the angle of a solid red radial line on the displaced body circle. This line extends from the planet center, so it will always connect to the mass center trajectory. The nominal rotational position is always indicated by a black dotted horizontal line. Elastic-body motion is depicted by blue dots (accelerometer locations in Fig. 6) connected by a spline interpolated thick red line. We are only able to obtain this data experimentally for the ring gear. In finite element modeling – without limitations on sensor placement – we also do this for the excited planet gear.

There are not enough data acquisition channels to measure all discrete-body and elastic-body degrees of freedom in experiments simultaneously. Only planet one (excited by the modal shaker in Fig. 2b) discrete-body motion is acquired when measuring the full elastic-body motion of the ring gear. This is what most experimental vibration shapes show. In the last mode considered we wish to understand the discrete-body motion of the carrier, sun gear, and another planet. In this case we can only partially measure the elastic-body motion of the ring gear with five accelerometers for that data set.

Fourier analysis is often applied to planetary gear analysis [57]. The elastic-body vibration shape of the ring gear (and a planet gear for one of the modes) can be represented as a Fourier series consisting of a sum of sinusoidal terms of the form $a_n \sin(n\theta + \phi_n)$, where such a term is referred to as the n-nodal diameter component [37]. The relative amplitudes of the Fourier series coefficients a_n from the vibration shapes are considered throughout this paper. Zero nodal diameter motion is a “breathing” mode where the entire ring expands/contracts together. The one nodal diameter component depicts rigid-body

translation. The two nodal diameter component is an ovular shape (two lobes). The three nodal diameter mode has three lobes, and so on.

3. Finite element/contact mechanics model

Experimental results are supported by a finite element/contact mechanics (FE/CM) model created in software developed by Vijayakar [58,59] and used previously [53,54]. This established modeling technique was compared successfully to experimental data from spur gear pairs [60] and planetary gears by Singh, Kahraman, and Ligata [50,61,62] and in our previous work [53]. Shweiki et al. [63] more recently presented a similar hybrid finite element/contact mechanics model compared against experiments on a spur gear pair. Dynamic finite element analysis of planetary gears is often too time-consuming because a highly-refined mesh is needed near moving contact points. The FE/CM model addresses this issue with an analytical contact mechanics formulation at tooth surfaces to improve computational speed and make dynamic simulation possible in reasonable time. More detail regarding the combined FE/CM model and computational efficiency of this technique is contained in [25]. A planar model is sufficient for the present spur planetary gear. The model predicts discrete-body vibrations of all gear components for direct comparison to the experiments for these degrees of freedom. The software outputs the deflection of any specified node. We use this tool to obtain the elastic deformation of 16 nodes on the ring gear coinciding with the experimental accelerometer locations in Fig. 6. Eventually the elastic-body motion of the excited planet also drew interest, so 16 nodes (with #1 pointed toward the sun gear in the $-x_p$ direction and numbered counterclockwise) are also probed around this gear body, as illustrated in Fig. 7.

The FE/CM model uses boundary conditions that simulate experimental conditions. Numerical values are contained in [53]. The rotational stiffnesses of the sun gear and carrier shafts (obtained analytically and by finite element analysis) are applied to the rotational degrees of freedom of those components, although our prior work [53] shows that these parameters do not affect the frequency range of current interest. The model applies experimentally measured translational stiffnesses of carrier and sun gear bearings. Similar stiffnesses acting on the discrete-body translational degrees of freedom of the ring gear models the ring gear fixtures. The ring gear is fixed rotationally to prevent kinematic drift, while the carrier and sun gear are free to rotate under the action of opposing torques that match experimental values. The radial stiffness of the interface between the ring gear and fixtures is simulated by increased elastic modulus of the outer ring gear elements, as described below.

Finite element modeling that captures accurate elastic-body vibration presents additional challenges. Only discrete-body motion was studied in previous work comparing experiments and finite element simulation, so the outer race of the ring

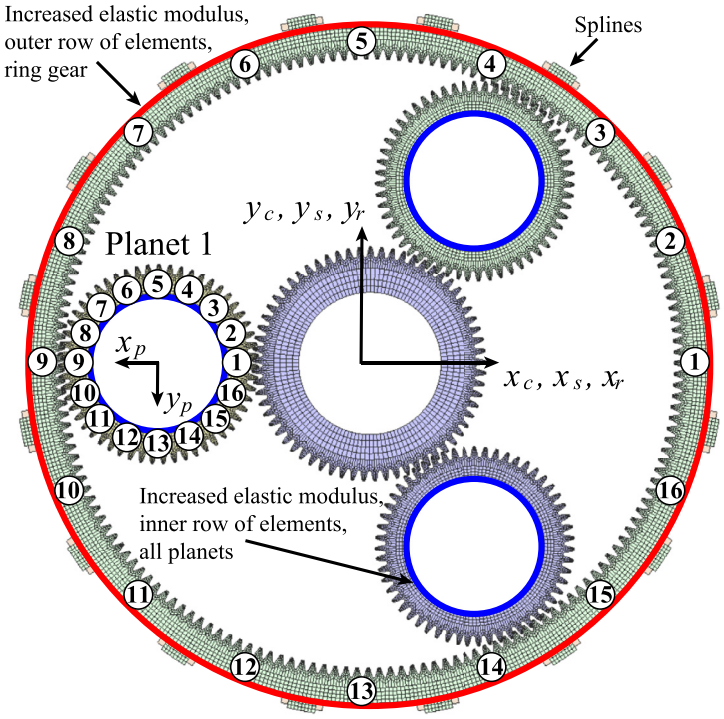

Fig. 7. Finite element/contact mechanics model of the three-planet system with 16 finite element node probes equally-spaced around the excited planet gear and ring gear.

Fig. 8. Experimental planet gear with duplex cylindrical roller bearing. The bearing outer race is the planet gear body, and the inner race is the solid planet pin (not shown).

gear and inner race of all external gears were defined rigid in [53]. That constraint must be lifted in light of the elastic-body vibration, but these surfaces are far from free. The experimental ring gear is restrained from elastic-body deformation by the snugged bolts holding it to the fixtures and a close slip fit with the fixture inner radius surface. The planet gears are restrained from elastic-body deformation by the distributed radial stiffness of their bearings shown in Fig. 8. Without any consideration of these stiffness factors, the FE/CM model drastically underestimates natural frequencies with significant elastic-body deformation. The elastic-body support stiffness of the ring gear and planet gears just mentioned is accommodated primarily by adjusting the elastic modulus of the mesh elements at the boundaries noted. The ring gear and planet gear rim meshes (sufficiently away from the tooth elements) in the FE/CM model each have four rows of elements. The stiffness resisting elastic-body deformation of the ring gear in the fixtures was captured by increasing the elastic modulus of the outermost row of ring gear elements by one order of magnitude, identified iteratively to bring FE/CM results into agreement with experiments. Ring gear splines are also used in the model to simulate the stiffness provided by the 16 bolts in the fixtures. Using similar correlation between FE/CM model results and experiments, the stiffness resisting elastic-body deformation of the planet gears in the bearings was captured by increasing the elastic modulus of the innermost row of planet gear elements by about two orders of magnitude. Fig. 7 illustrates these FE/CM model features.

It is also necessary to account for additional mass and inertia of gear bodies not represented in the finite element mesh. The facewidth of each gear component is thinner than its main body. The FE/CM model uses the facewidth to define the axial thickness of elements, so the additional mass of the thicker gear bodies must be represented separately. Starting from our original work in [53], we have used the width of the gear teeth in the FE/CM model plus an additional lumped mass/inertia attached to each gear component that accounts for the material in thicker areas of the gear bodies and the added mass/inertia of the planet gear adapter flanges in Fig. 4b for those components.

3.1. Finite element/contact mechanics model data processing

Dynamic time-based simulation is computationally expensive, so computer simulation mimicking the experiments – where steady state response is obtained across hundreds of frequency steps – would be highly time-consuming. Instead, the impulse response from a stimulus at the experimental shaker attachment point is obtained for all degrees of freedom. The impulse simulation consists of four ranges: (1) a single static time step to preload the system, (2) a four time step ramp up with increasing force/torque on the experimentally excited planet gear, (3) a three step ramp back down to the static load, and (4) an 8192 step free vibration response with only the mean load. Every time step is 0.000025 sec. The Fourier transform of the time response in the last range gives a frequency response function (FRF) for direct comparison against the experimental results. Mode vibration shapes are obtained from the magnitude/phase information of each degree of freedom (discrete-body or elastic-body) from these FRF plots, as in [53]. This method reliably produces the mode shape when modes are well-spaced and lightly damped. Vibration shapes presented from the finite element model will always contain the discrete-body motion of all planets, sun gear, and carrier, along with the elastic-body motion of the ring gear and excited planet gear.

4. Elastic-body vibration: experiments and simulation

Experiments were originally designed to collect lumped-parameter rotational/translational data to compare against computer models [53] and study the sensitivity of vibration response to key parameters [54,64]. Accelerometers were mounted to planets and central members in orientations that accomplish these measurements. Little attention was devoted to ring gear motion in [53], considering its firm support. In later data processing, however, additional modes not predicted by the analytical model were discovered in the measured ring gear and planet gear vibration. At that point there was already

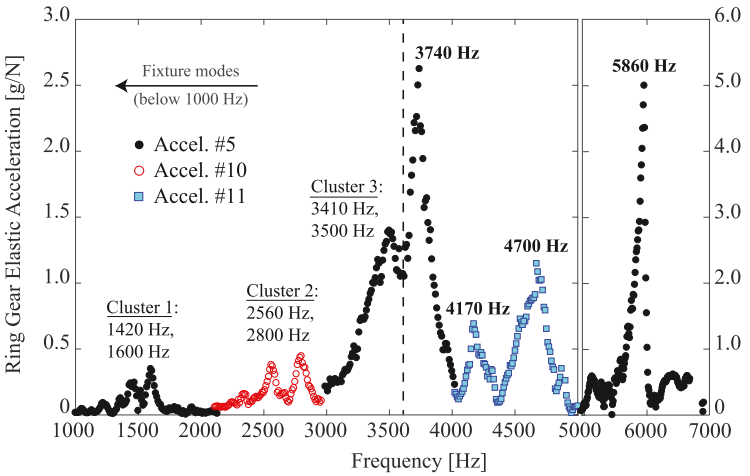

Fig. 9. Shaker testing experimental frequency response of the three-planet system for ring gear accelerometer #5 (solid black circle), 10 (open red circle), and 11 (blue square) in Fig. 6. (For interpretation of the references to colour in this figure legend, the reader is referred to the web version of this article.)

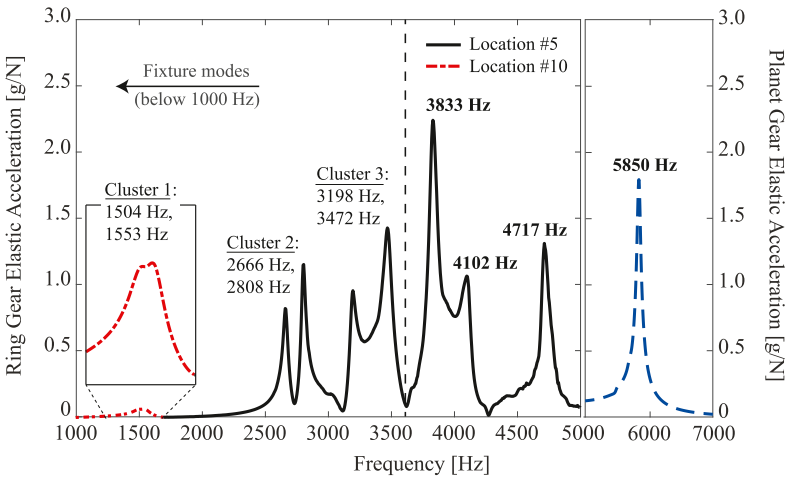

Fig. 10. FE/CM model impulse frequency response of the three-planet system using ring gear locations #5 (solid black) and 10 (dash-dot red) along with planet gear elastic vibration (blue dash) at higher frequencies. (For interpretation of the references to colour in this figure legend, the reader is referred to the web version of this article.)

strong discrete-body agreement between the models and experiments, as presented in [53], so we hypothesized that the additional modes contained significant elastic-body motion that would not be captured in the lumped-parameter model. The data presented here shows this to be true. Additionally, the gear modes previously assumed to be characterized completely by discrete-body motion and successfully correlated to a lumped-parameter model also demonstrate elastic-body ring gear deformation. This paper differentiates these two categories: (1) modes previously identified and successfully compared to a lumped-parameter model that we now realize also contain elastic-body motion, and (2) elastic-body modes not identified by lumped-parameter modeling. We believe that the lumped-parameter model predicted the former because those modes have a larger portion of their strain and kinetic energy associated with lumped-parameter elements, so we call them "moderately elastic-body modes." Modes in the latter category have a significant portion of energy associated with elastic-body vibration, so we call them "dominantly elastic-body modes." There is no quantitative criterion to distinguish modes in the two categories noted, except moderately elastic-body modes have enough discrete-body motion that a lumped-parameter model identifies them, albeit incompletely, with reasonable accuracy, while dominantly elastic-body modes are missed by the analytical model.

Fig. 9 shows the experimental frequency response in the radial direction of the ring gear using the three accelerometer locations identified in Fig. 6. Three locations are used in the plot because different locations around the ring gear demonstrate each resonant peak better than others due to the nature of elastic continuum deformation. A given accelerometer location may exhibit maximum elastic-body deflection (if near an anti-node) or zero deflection (if close to a vibration node). The vertical dashed line around 3600 Hz in Fig. 9 separates the region of previously-studied "gear modes" (in [53,54]) to the

Table 2
Natural frequencies of modes with elastic-body vibration from shaker testing experiments (Fig. 9) compared to the finite element/contact mechanics model (Fig. 10).

Mode	Relationship	Experiments	FE/CM Model	Error
13	*Cluster 1*	1420 Hz	1504 Hz	5.9%
14	*Cluster 1*	1600 Hz	1533 Hz	−2.9%
15	*Cluster 2*	2560 Hz	2666 Hz	4.1%
16	*Cluster 2*	2800 Hz	2808 Hz	0.3%
17	*Cluster 3*	3410 Hz	3198 Hz	−6.2%
18	*Cluster 3*	3500 Hz	3472 Hz	−0.8%
19	*Elastic Ring Dominant*	3740 Hz	3833 Hz	2.5%
20	*Elastic Ring Dominant*	4170 Hz	4102 Hz	−1.6%
21	*Elastic Ring Dominant*	4700 Hz	4717 Hz	0.4%
22	*Elastic Planet Dominant*	5860 Hz	5850 Hz	−0.2%

left and modes not previously identified to the right. Prior work [64] characterized the discrete-body gear modes into three clusters, an identification tool that is used here too. Each cluster is a group of modes with similar natural frequency. Each mode within a given cluster is dominated by similar planet motion: radial translation in one cluster, tangential translation in another cluster, and rotation in the remaining cluster. The number of modes in each cluster depends on the number of planets. A three-planet system, most commonly used in this paper, has two modes in each cluster, one rotational mode and one translational mode (descriptions which refer to central member vibration [13]). The gear modes were thought to be accurately described in terms of discrete-body motion only, and past publications focused on discrete-body motion of the planets, sun gear, and carrier. There are, in addition to the gear modes below 3600 Hz, four more frequency response peaks at higher frequency not previously identified because they exhibit elastic-body motion, primarily in the ring gear. The 5860 Hz mode (number 22 in Table 2) also features planet elastic-body motion, as we will describe.

Fig. 10 shows the FE/CM simulation results of essentially the same data. Node/accelerometer location #11 is not used (it is right next to #10, see Fig. 6). Additionally, planet gear data helps identify the highest mode (5850 Hz in this figure). Planet gear motion is dominant in experiments in this mode too. Natural frequencies and relative amplitudes in the experiments and FE/CM model are remarkably similar. Table 2 compares the natural frequencies in Figs. 9 and 10. The mode numbers start at 13 because the first 12 modes were previously identified as “fixture modes” with predominant strain energy in the shafts and supporting bearings [53]. All natural frequencies in Table 2 agree within 6% error, and 70% of them agree within 3% error. Modes 13 through 18 in the three clusters are the moderately elastic-body gear modes to the left of the vertical dashed line in Figs. 9 and 10. Modes 19 through 22, are dominantly elastic-body. Unless specifically noted that a natural frequency is in reference to the FE/CM model, we use the experimental frequency value. For example, the first mode with dominant ring gear elastic-body motion (number 19 in Table 2) will generally be called “the 3740 Hz mode.”

5. Moderately elastic-body modes

Gear modes 13 through 18 in Table 2 and to the left of the vertical dashed line in Figs. 9 and 10 were identified previously as discrete-body modes in [53] and [54], but that assumption of purely discrete-body vibration is shown below to not truly hold. The following results depict the elastic-body motion in these modes, focusing on ring gear nodal diameter components. Fig. 11 identifies the dominant elastic-body motion within these three clusters from experiments. The numbers on the horizontal axis are the nodal diameter components discussed at the end of Section 2.2 on experimental data processing. The similarity of ring gear deformation in terms of nodal diameter components within each cluster may be a property of clustered modes, but this is unexpected from analytical formulation in [37] that predicts different dominant nodal diameter components for rotational and translational modes. Each experimental cluster has one rotational mode and one translational mode, as described in [54], so we do not expect similar ring gear nodal diameter components within a cluster. Perhaps inter-modal interference is contributing to the experimentally observed similarity within clusters. The modes within each cluster are not widely spaced, especially clusters 1 and 3 in Fig. 9, so perhaps the ring gear deformation of one mode is dominating the vibration shape of the other. For now we focus on describing what is experimentally measured.

Ring gear elastic-body vibration in cluster 1 is dominated by two nodal diameter motion (which we expect in the translational mode for a system with three planets based on [37]), with a zero nodal diameter component also appearing in the 1420 Hz mode. Cluster 2 has primarily one nodal diameter motion, which is discrete-body motion. Experiments show minimal elastic-body motion in this cluster. Ring gear elastic-body vibration in cluster 3 is dominated by three nodal diameter and zero nodal diameter motion (which we expect in a rotational mode for a system with three planets). Although natural frequencies and relative amplitude peaks agree well between the experiments and FE/CM model in Table 2 and Figs. 9 and 10, there is less agreement between the experiments and the model when analyzing the vibration shape of the ring gear within these modes. For example, experiments show little elastic-body motion in cluster 2, but the FE/CM model shows significant elastic-body motion. Key similarities and differences are highlighted in the following sections.

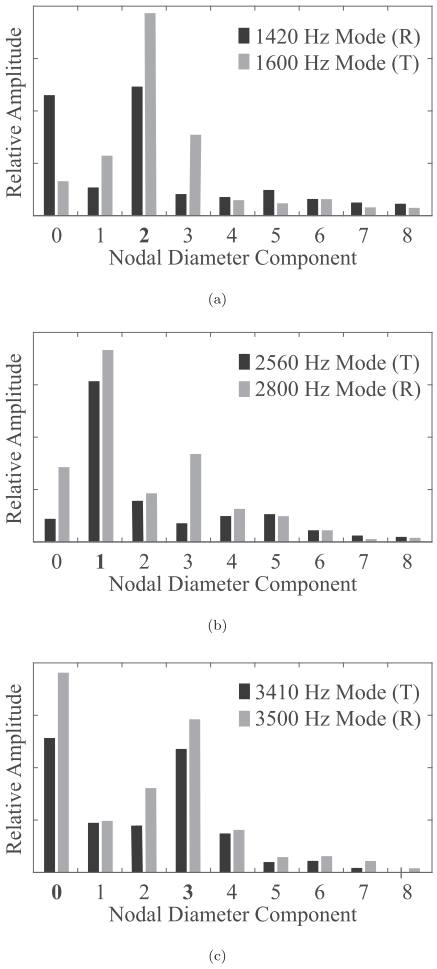

Fig. 11. Relative amplitude of ring gear elastic-body nodal diameter components in gear modes from experiments for (a) cluster 1, (b) cluster 2, and (c) cluster 3.

5.1. Cluster 1 (modes 13 and 14)

Fig. 12 shows the experimental vibration shapes of the 1420 Hz and 1600 Hz modes in cluster 1. The two nodal diameter component of vibration is demonstrated in both but is stronger in the 1600 Hz mode, a translational mode according to [54]. Two nodal diameter ring gear elastic-body vibration is analytically predicted in [37] for a translational mode. This mode has the higher response amplitude, of these two, in Fig. 9. The FE/CM model shows minimal elastic-body vibration

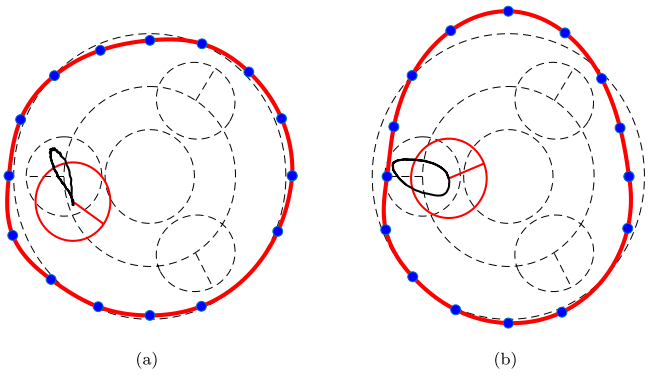

Fig. 12. Vibration shapes of cluster 1 modes, (a) 1420 Hz (number 13) and (b) 1600 Hz (number 14), with discrete-body motion of the excited planet gear and elastic deformation of the ring gear (blue dots) from experiments. (For interpretation of the references to colour in this figure legend, the reader is referred to the web version of this article.)

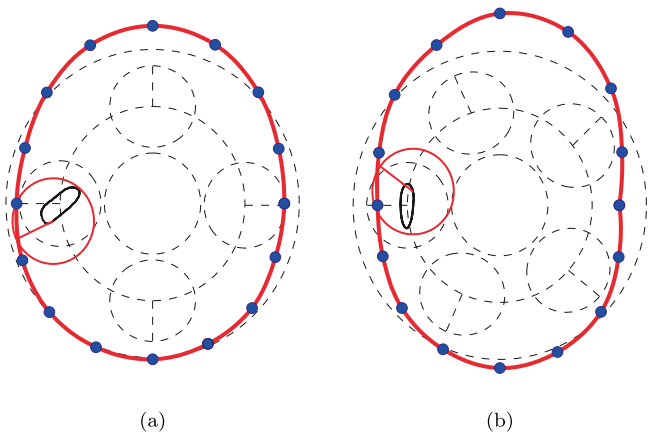

Fig. 13. Vibration shape of the second cluster 1 mode (number 14) in (a) the four-planet gear system at 1520 Hz and (b) the five-planet gear system at 1440 Hz with discrete-body motion of the excited planet gear and elastic deformation of the ring gear (blue dots) from experiments. (For interpretation of the references to colour in this figure legend, the reader is referred to the web version of this article.)

in these modes (note the low cluster 1 amplitudes in Fig. 9). It is understandable that these modes were predicted by the lumped-parameter model in [53] and [54] because the elastic-body motion is not prominent compared to discrete-body degrees of freedom, but it is clearly present.

Additional planet configurations: Ring gear elastic-body behavior also appears when the system is assembled in different planet configurations. Figs. 13a and 13b show the 1600 Hz mode in the four-planet and five-planet configurations, respectively. All components in the four-planet and five-planet experiments are identical to those for three-planet experiments except for the carrier. The existence and character (dominant two nodal diameter component) of elastic-body motion is independent of the number of planets. The natural frequencies are similar among the three systems. The natural frequency of the 1600 Hz mode decreases with additional planets, first by 5.0% on increasing from three to four planets (1520 Hz), then an additional 5.2% on increasing from four to five planets (1440 Hz).

5.2. Cluster 2 (modes 15 and 16)

Fig. 11 b shows minimal elastic-body ring gear vibration in cluster 2 from experimental measurements. The one nodal diameter component is dominant, and this component represents discrete-body translational motion where the ring gear moves as a rigid body. The FE/CM model, however, shows interesting elastic-body motion in this cluster. Fig. 14 shows the vibration shapes for cluster 2 modes from computer simulation. The magnitude A and phase ϕ of the translational components of 16 ring gear nodes and 16 planet gear nodes highlighted in Fig. 7 are calculated from the impulse response to animate the elastic motion of these components by plotting $A\sin(\omega t+\phi)$ for each of finite element node. The deflected ring gear shape has four lobes in the 2666 Hz mode and three lobes in the 2808 Hz mode. Fig. 14c confirms that the ring gear vibration in these modes is principally in the four and three nodal diameter components, respectively.

It is unclear why the experiments show minimal elastic-body vibration in cluster 2, but the FE/CM model has interesting deformation. As noted, although natural frequencies and resonant amplitudes agree well between the experiments and model (Figs. 9 and 10), there is less agreement in the vibration shapes. Our method of increasing the stiffness of the outer ring gear elements to model the support structure stiffness is an approximation, as is a similar modeling approach for the planet bearing stiffness. The irregular spacing of ring gear mounting holes and housing geometry is not taken into account. In addition, lumped mass is added to the ring gear to account for its varying radial thickness. It appears the natural frequencies are more forgiving of these modeling approximations than the mode shapes, as expected in general for vibrating systems.

The nodal diameter components in Fig. 14 agree with analytical predictions in [37]. From magnified central member motions, and prior publication [54], the 2666 Hz mode (number 15) is a translational mode and the 2808 Hz mode (number 16) is a rotational mode. Wu and Parker predict the four nodal diameter component in the former and the three nodal diameter component in the latter. Thus the FE/CM results agree with prior analytical work.

5.3. Cluster 3 (modes 17 and 18)

Fig. 15 shows the experimental vibration shapes of the 3410 Hz and 3500 Hz modes in cluster 3. They feature a strong three nodal diameter component of vibration in the ring gear, as noted in Fig. 11(c). The two vibration shapes look similar in Fig. 15, but these are two distinct modes. One is a rotational mode and the other a translational mode, as defined by Lin and Parker [13] and Wu and Parker [37]. The differences are contained in the motion of the carrier and sun gear, which are not measured in this data set due to data acquisition limitations. The similarities in ring gear elastic-body vibration, however,

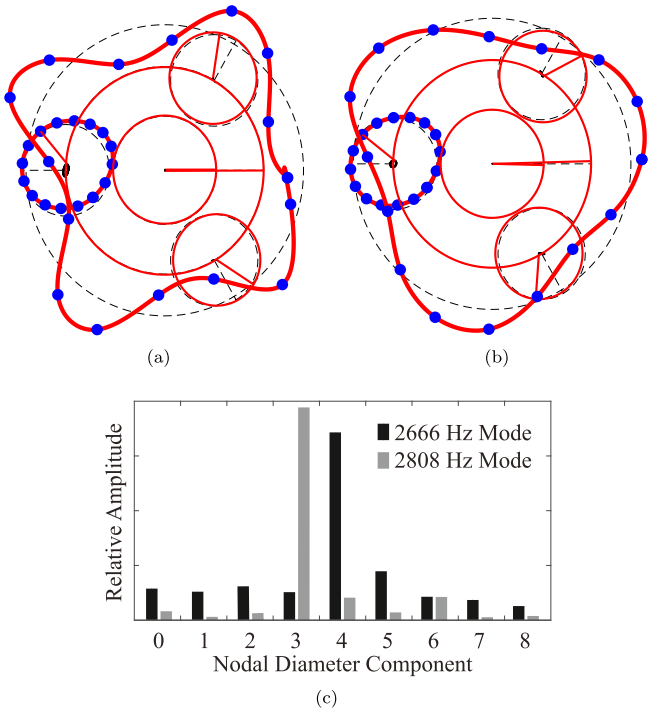

Fig. 14. Vibration shapes of cluster 2 modes, (a) 2666 Hz (number 15) and (b) 2808 Hz (number 16), with discrete-body motion of all components and elastic deformation of planet 1 and the ring gear (blue dots), and (c) relative amplitude of ring gear elastic-body nodal diameter components in these modes (black: 2666 Hz and gray: 2808 Hz) from FE/CM simulation. (For interpretation of the references to colour in this figure legend, the reader is referred to the web version of this article.)

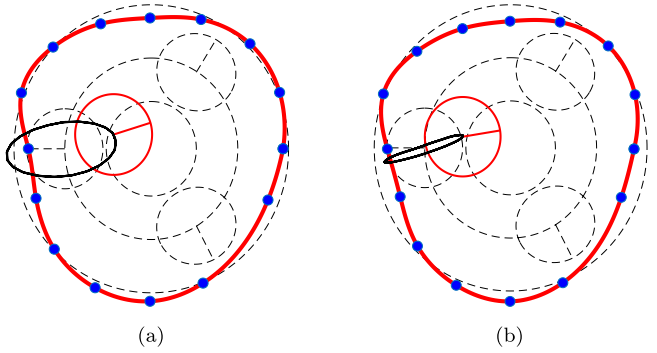

Fig. 15. Vibration shapes of cluster 3 modes, (a) 3410 Hz (number 17) and (b) 3500 Hz (number 18), with discrete-body motion of the excited planet gear and elastic deformation of the ring gear (blue dots) from experiments. (For interpretation of the references to colour in this figure legend, the reader is referred to the web version of this article.)

may be a case of inter-modal interference, considering the closeness of these two modes in Fig. 9. The FRF shows a dominant peak in the 3500 Hz mode (number 18). According to [54], this is a rotational mode and [37] analytically predicts the three nodal diameter component for this mode type. It is likely that the 3500 Hz mode is captured accurately but is affecting the results for the 3410 Hz mode that has lower vibration amplitude.

The FRF from the FE/CM model in Fig. 10 shows better spacing between modes 17 and 18 in cluster 3. As a result, the vibration shape for mode 17 is distinct from mode 18 in computer simulation results. Fig. 16 shows the vibration shape in this first cluster 3 mode and the relative amplitude of its nodal diameter components. This is a translational mode from [54], and [37] analytically predicts the four nodal diameter component for this mode, agreeing with the FE/CM results in Fig. 16.

We see that experiments and the FE/CM model show moderate elastic-body ring gear deformation in all three gear mode clusters that were previously thought to be exclusively discrete-body modes containing no elastic continuum deformation. Natural frequencies and vibration amplitudes agree well between the experiments and FE/CM model. The deformed ring gear shapes differ in some cases, likely due to inter-modal interference or because FE/CM model approximations do not capture

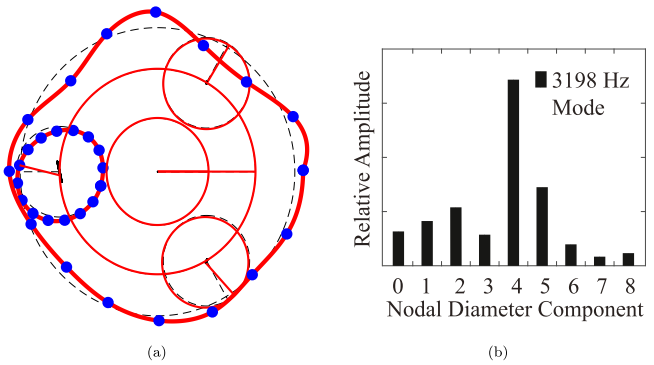

Fig. 16. Planetary gear (a) vibration shape and (b) ring gear elastic-body nodal diameter components of the first cluster 3 mode, 3198 Hz (number 17), from FE/CM simulation.

some details of the experimental setup. These approximations are difficult to eliminate. Because previous lumped-parameter model results (natural frequencies) matched well for these modes, we conclude that they are characterized mostly in terms of discrete-body motion, but they clearly involve elastic-body motion in the ring gear. The lumped-parameter model may predict the natural frequencies, but a full description of the mode shapes is not achievable without consideration of the distributed elastic properties of the ring gear.

6. Dominantly elastic-body modes

The four dominantly elastic-body modes to the right of the vertical dashed line in Figs. 9 and 10 were not identified in previous research or by a lumped-parameter model. The nature of this condition implies that these modes have a larger portion of their energy in motion that is only captured by considering elastic-body motion with a distributed-parameter model of the planetary gear, mostly the ring gear.

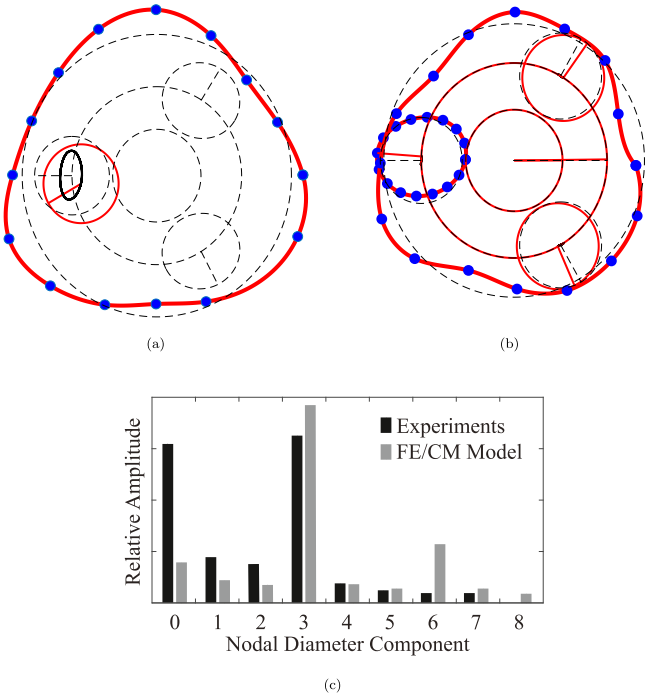

Fig. 17. Vibration shape of the first dominantly elastic-body mode (number 19) at (a) 3740 Hz from experiments and (b) 3833 Hz from FE/CM simulation, and (c) relative amplitude of ring gear elastic-body nodal diameter components in each vibration shape (black: experiments and gray: FE/CM simulation).

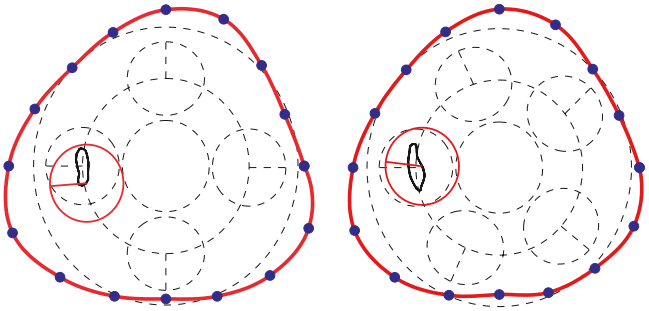

Fig. 18. Vibration shape of mode 19 in (a) the four-planet gear system at 3800 Hz and (b) the five-planet gear system at 3840 Hz with discrete-body motion of the excited planet gear and elastic deformation of the ring gear (blue dots) from experiments. (For interpretation of the references to colour in this figure legend, the reader is referred to the web version of this article.)

6.1. First dominantly elastic-body mode: 3740 Hz in experiments (mode 19)

The first dominantly elastic-body mode was measured at 3740 Hz in experiments and 3833 Hz in FE/CM simulation, a 2.5% error. The experimental and FE/CM simulation vibration shapes agree well for this mode. They both exhibit dominant three nodal diameter elastic vibration in the ring gear. Fig. 17 shows the vibration shape at this mode from (a) experiments and (b) FE/CM simulation. Fig. 17c shows the relative amplitude of ring gear elastic-body nodal diameter components for this mode from experiments and FE/CM simulation which both have elastic-body deformation characterized predominantly by a three nodal diameter component. FE/CM simulation also shows some six nodal diameter contribution. Experiments show noticeable zero nodal diameter content, a “breathing” motion in which the whole ring expands and contracts uniformly.

Additional planet configurations: Similar to the 1600 Hz mode in cluster 1 considered earlier, measurements of the 3740 Hz mode were collected when the system is assembled with additional planets. Figs. 18a and 18b show this mode in the four-planet and five-planet configurations, respectively. The natural frequency of the 3740 Hz mode increases with additional planets, first by 1.6% on increasing from three to four planets (3800 Hz), then an additional 1.1% on increasing from four to five planets (3840 Hz). As with the 1600 Hz mode, the elastic-body deformation of the ring gear in the 3740 Hz mode is consistently dominated by the three nodal diameter component with three, four, and five planets.

6.2. Second and third dominantly elastic-body modes: 4170 Hz and 4700 Hz in experiments (modes 20 and 21)

The second dominantly elastic-body mode was measured at 4170 Hz in experiments and 4102 Hz in FE/CM simulation, a -1.6% error. The third dominantly elastic-body mode was measured at 4700 Hz in experiments and 4717 Hz in FE/CM simulation, a 0.4% error. There is not one dominant nodal diameter component in these modes; many components are active. Fig. 19 shows the vibration shapes of the second (4170 Hz) and third (4700 Hz) dominantly elastic-body modes from FE/CM simulation. Additionally, Fig. 19c shows the relative amplitude of ring gear elastic-body nodal diameter components for these modes. Elastic-body deformation of the ring gear is dominant in these modes.

6.3. Fourth dominantly elastic-body mode: 5860 Hz in experiments (mode 22)

The last mode to consider is qualitatively different than all modes discussed above where the meaningful elastic-body motion is primarily in the ring gear. The 5860 Hz mode features significant elastic-body motion of the measured planet gear in addition to the experimentally measured ring gear vibration demonstrated in Fig. 9. For this reason, and because the measured vibration amplitudes are high, we will look more closely at this mode.

Fig. 20 shows the experimental frequency response of planet rotational acceleration for the shaker-excited planet gear during modal vibration experiments in the three-planet configuration. The gear modes analyzed previously [53] are observed to the left of the vertical dashed line, as before. The first three dominantly elastic-body modes, which feature deformation in the ring gear, do not appear strongly in planet discrete-body rotation. Fig. 20 does, however, illustrates the significance of the 5860 Hz mode with its high amplitude. Response at this frequency is highest in the planet gear, followed by radial ring gear vibration in Fig. 9. At higher torque there is increased discrete-body motion of the carrier. The lower vibration amplitude of other gear bodies and absence of any discrete-body modes predicted by analytical modeling in this frequency vicinity suggests that this mode is dominated by elastic-body vibration of the planet gear coupled with elastic-body ring gear vibration and, at higher torque, discrete-body carrier vibration.

Additional planet configurations: The planetary gear was assembled and tested in four-planet and five-planet configurations to see if the 5860 Hz mode remains so prominent with different planet numbers. Fig. 21a shows the rotational vibration of the planet gear excited by the modal shaker in the four-planet configuration, and Fig. 21b shows the same re-

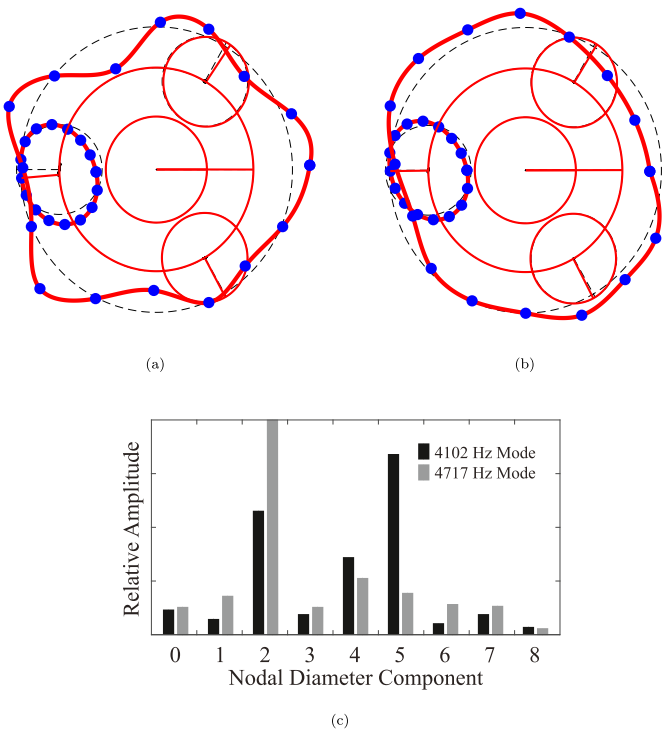

Fig. 19. Vibration shapes of the second and third dominantly elastic-body modes at (a) 4102 Hz (mode 20) and (b) 4717 Hz (mode 21), respectively, with rigid-body motion of all components and elastic deformation of planet 1 and ring gears (blue dots), and (c) relative amplitude of ring gear elastic-body nodal diameter components in these modes (black: 4102 Hz and gray: 4717 Hz) from FE/CM simulation. (For interpretation of the references to colour in this figure legend, the reader is referred to the web version of this article.)

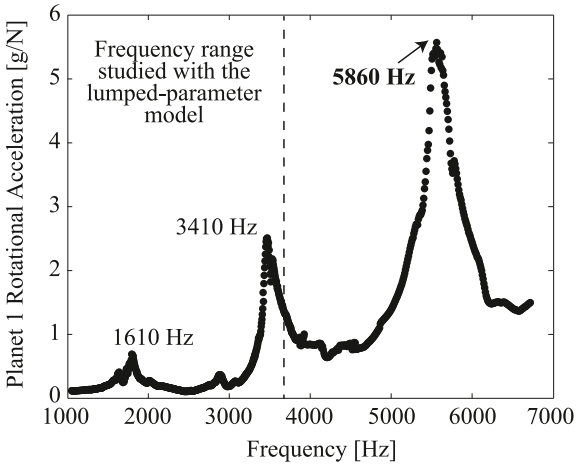

Fig. 20. Shaker testing experimental frequency response of the three-planet system for planet 1 rotational acceleration with shaker excitation on the planet gear body parallel to the line of action with the ring gear. The applied torque is 68 N-m at the sun gear.

sult in the five-planet configuration. The static load was increased accordingly in these configurations to maintain similar load distribution per planet gear. High-amplitude peaks associated with this mode are evident in each of the three-planet, four-planet, and five-planet configurations, although the resonant frequency varies slightly across the three cases. The frequency of the four-planet peak is 3.9% greater than the three-planet peak, and the five-planet peak is 2.4% less than the three-planet peak. Clearly the mode persists for differing number of planets.

Multiple elastic-body modes have been identified in three-planet, four-planet, and five-planet systems with small variation in natural frequency. This has been demonstrated in moderately elastic-body mode 14 (cluster 1), ring gear dominantly elastic-body mode 19 (3740 Hz), and planet gear dominantly elastic-body mode 22 (5860 Hz). Elastic-body vibration is prevalent across systems with varying number of planet gears.

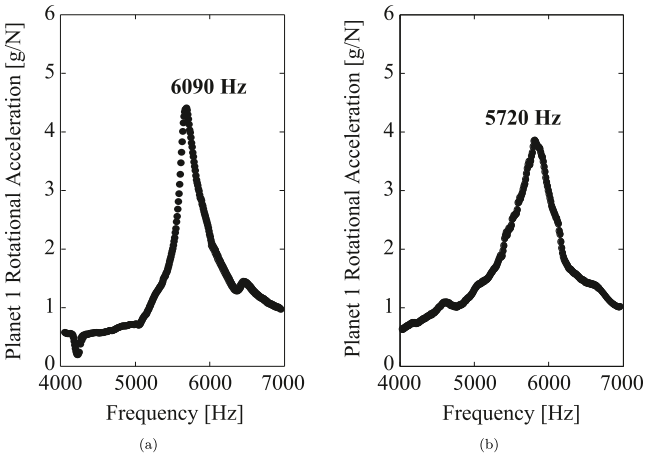

Fig. 21. Shaker testing experimental frequency response of (a) four-planet and (b) five-planet systems for planet 1 rotational acceleration with shaker excitation on the planet gear body parallel to the line of action with the ring gear. The applied torque is 102 N-m in the four-planet system and 136 N-m in the five-planet system at the sun gear.

6.3.1. Discrete-body motion of the 5860 Hz mode

Fig. 22 shows the experimental discrete-body vibration (one rotational and two translational degrees of freedom) of the shaker-excited planet gear for the 5860 Hz mode at six different torques. The planet gear is in the 9 o'clock position on the carrier, as shown in Figs. 6 and 7. The equilibrium position of the planet gear is illustrated by dashed lines. The horizontal dashed line (9 o'clock orientation) indicates rotational equilibrium, and the solid radial line indicates rotational vibration amplitude. The solid planet gear circle illustrates the deflected position of the planet gear at maximum rotational vibration (the degree of freedom shown in Figs. 20 and 21). Each of the six images shows a snapshot in time of the rotational/translational vibration with the planet gear circle and radial rotation line. In addition, the trajectory of the planet center through time is traced by a thick black line. This orbital path is defined by planet discrete-body translational vibration, which is small at lower torque. As torque increases, translational deflections (and the size of the orbital path) increase. The major axis of the path rotates clockwise, indicating a change in phase between the x_p and y_p translational vibration components. The maximum rotational amplitude increases slightly at higher torque. Most importantly, Fig. 22 shows that higher torque increases the tangential y_p translational discrete-body vibration of the planet gear that interacts strongly with the carrier.

Initial observations at low torque (68–136 N-m at the sun gear in Figs. 20 and 21) exhibited small central member (sun gear and carrier) vibration in the 5680 Hz mode. Fig. 22, however, shows increased discrete-body planet translational motion

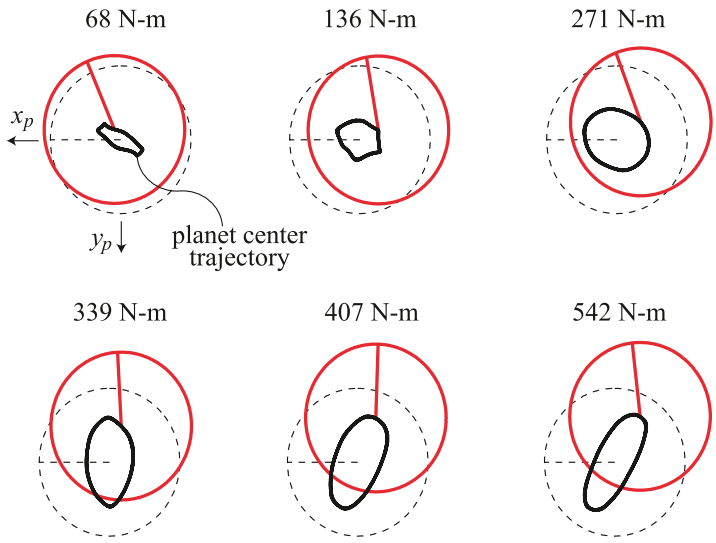

Fig. 22. Planet gear orbit paths in experimental shaker tests on the three-planet gear system at various sun gear input torques. The planet gear is shown at the instance of maximum rotational vibration. Shaker excitation is on the planet gear body parallel to the line of action with the ring gear. The excitation frequency is at the 5860 Hz mode (number 22). The orbit trajectories move counterclockwise at all torque levels. The applied torque is given for each case.

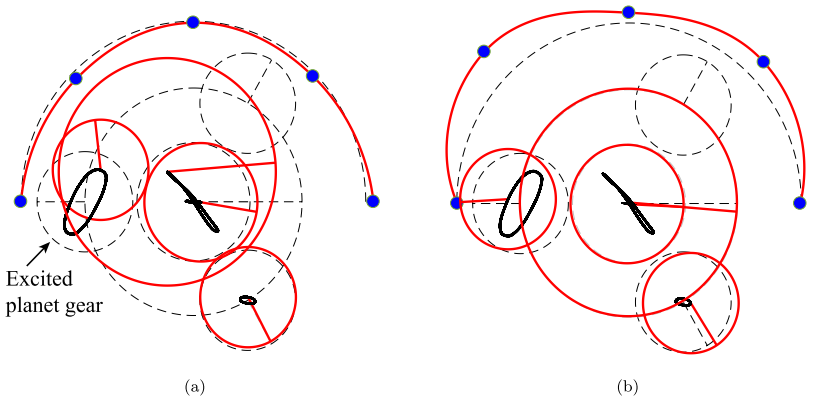

Fig. 23. Discrete-body motion of two planets, sun gear, and carrier along with elastic-body motion of half the ring gear at 5860 Hz from experimental acceleration response under steady state excitation of the three-planet gear system with a quarter of a vibration cycle phase shift between the two images in (a) and (b). Shaker excitation is on the planet gear body parallel to the line of action with the ring gear. The applied torque is 542 N-m at the sun gear.

at higher torque, and this vibration couples with carrier motion. Fig. 23 shows the experimentally measured vibration shape at 5860 Hz with 542 N-m torque at the sun gear, the highest experimental load applied. This figure shows the discrete-body rotational/translational motion of the excited planet gear, sun gear, carrier, and one other planet gear. It also shows the radial elastic-body deformation of half the ring gear with five accelerometer measurement points located by the solid dots[3] The evident ring gear elastic-body vibration of this mode is discussed in more detail in the next section. Dashed lines indicate the equilibrium position of the planetary gear with the straight ones showing the nominal rotational position of planets and central members. The lines for sun gear and carrier rotational equilibrium are horizontal in the 3 o'clock position. The magnitude of discrete-body rotational vibration of the central members and two planet gears is indicated by a solid line for each body. As in Fig. 22, this line is tied to the mass center trajectory of each of the four discrete-body components, although the sun gear orbit is too small to see. The carrier trajectory is almost a diagonal line, indicating in-phase vibration and little damping in this component.

As before, the images in Fig. 23 are created by animating the measured vibration from accelerometers during steady-state excitation of the 5860 Hz mode and taking snapshots at instances in time through a vibration period. All vibration amplitudes are equally magnified. As mentioned, sun gear vibration is small. There is also little carrier rotation (its line for this degree of freedom remains nearly horizontal). Carrier translation is the most prominent central member vibration. Thus, with sufficient torque, the active discrete-body degrees of freedom in the 5680 Hz mode are planet rotation, planet translation, and carrier translation. The translational degrees of freedom are less active at low torque.

The next section focuses on elastic-body motion of this mode, but Fig. 23 illustrates an interesting relationship between the discrete-body degrees of freedom (planets and central members) and the elastic-body motion of the ring gear for this mode. Maximum discrete-body rotational/translational vibration amplitude of the excited planet and central members (Fig. 23a) coincides with minimal ring gear deflection, and maximum ring gear deflection (Fig. 23b) coincides with minimal discrete-body vibration of the excited planet gear and central members. Overall, maximum discrete-body deflections (dominated by the excited planet gear and carrier) tend to be 90^o out-of-phase with maximum elastic-body deflections. This phase difference likely arises from damping.

6.3.2. Elastic-body motion of the 5860 mode

The 16 radially-mounted accelerometers in Fig. 3 measure the elastic-body vibration of the ring gear at this mode in greater detail than in Fig. 23. Fig. 9 shows that ring gear elastic-body motion is prominent in this mode. As before, measurements can not be made simultaneously on the sun ear, carrier, and second planet when the additional ring gear accelerometers are active.

Fig. 24 a shows the experimentally measured discrete-body vibration of the shaker-excited planet gear and the elastic-body vibration of the ring gear from the 16 accelerometers[4] Planet elastic-body motion is not captured experimentally, but subsequent FE/CM simulations show that motion is prominent. Fig. 24b illustrates the relative amplitudes of ring gear nodal diameter components from experiments. Although significant elastic-body vibration is present in the ring gear, it is a mixture of several nodal diameter components. Figs. 23 and 24 show coupling between the planet and ring gears in the 5860 Hz mode. In these experiments, the ring gear is mounted to the gearbox housing with 16 bolts as shown in Figs. 3 and 6. These vibrations could easily transfer to the surrounding support structure of the gear in practical designs, transmitting noise and generating additional cyclical loads.

[3] There are not enough DAQ channels to simultaneously measure all 16 ring gear accelerometers and the accelerometers needed to capture the discrete-body rotational/translational motion of the other gears (four each).

[4] Except accelerometer #15, which was not working properly.

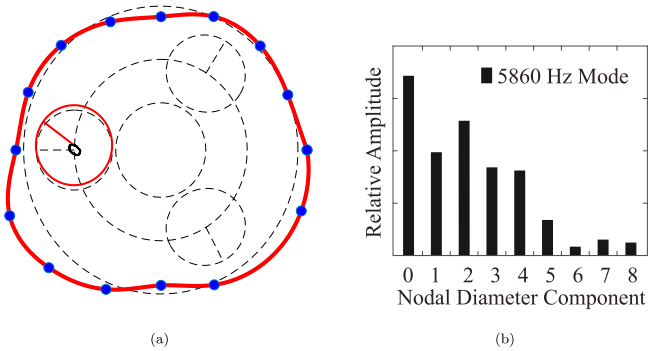

Fig. 24. Planetary gear (a) vibration shape with planet discrete-body motion and ring gear elastic-body motion (blue dots) and (b) associated ring gear elastic-body nodal diameter components at the 5860 Hz mode (number 22) from experiments. (For interpretation of the references to colour in this figure legend, the reader is referred to the web version of this article.)

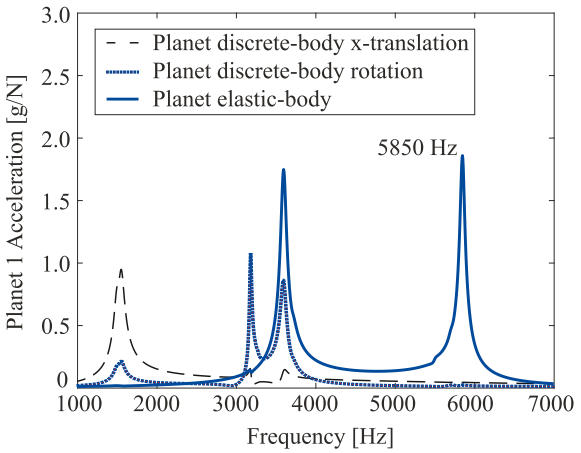

Fig. 25. FE/CM model discrete-body (black dash and red dot) and elastic-body (solid blue) impulse frequency response of planet 1 acceleration with excitation applied to simulate the modal shaker tests with 68 N-m at the sun gear. (For interpretation of the references to colour in this figure legend, the reader is referred to the web version of this article.)

The predominance of discrete-body planet gear motion (Figs. 20 and 21) in this higher-frequency mode suggests that elastic-body motion may be occurring in the planet in addition to the ring gear. Experimental measurements to support this are not possible, but a finite element natural frequency analysis of an unconstrained planet gear extracted from the full planetary gear model shows that it has a two nodal diameter elastic continuum mode in this frequency range. The full FE/CM model reveals this to be a prominant feature of the 5860 Hz mode. The planar elastic-body deflections at 16 mesh nodes equally-spaced around the planet gear are obtained using finite element probes, as noted in Fig. 7, just like on the ring gear in prior experiments and simulations. Fig. 25 shows the FE/CM discrete-body (rotational and translational) and elastic-body acceleration frequency response functions of the excited planet gear from a combined torque/force impulse to the experimentally excited planet gear. The combination of a force and torque input simulates the effect of the shaker mounted along the ring-planet line of action in experiments and excites modes with rotational and translational motion. The discrete-body curves show dynamic response primarily in the gear modes below 4000 Hz that are also evident in Figs. 20 and 21, and expected from prior research [53]. The discrete-body curves do not show a significant peak anywhere near 5860 Hz (mode 22). On the other hand, the elastic-body curve in Fig. 25 shows resonance at 5850 Hz, which indicates elastic-body vibration of the planet gear in this mode.

Fig. 26 shows the planetary gear vibration shape and associated nodal diameter components in the fourth elastic-body mode from the FE/CM model. The simulation shows that planet elastic-body vibration is much more prominent than ring elastic-body motion in this mode. The two nodal diameter component of the planet gear dominates the response. The most prominent component of the ring gear, the one nodal diameter component, is discrete-body motion. Comparing the vibration shape from FE/CM simulations in Fig. 26 to the experimental shapes in Figs. 23 and 24a is not practical because the most dominant motion in simulations – elastic-body motion of the planet gear – is not measurable in experiments. The ring gear, however, provides an opportunity for comparison. Experiments show more elastic-body ring gear motion (Fig. 24b) but FE/CM simulations indicate more discrete-body motion (Fig. 26b). Comparing the vibration shape of the fourth dominantly

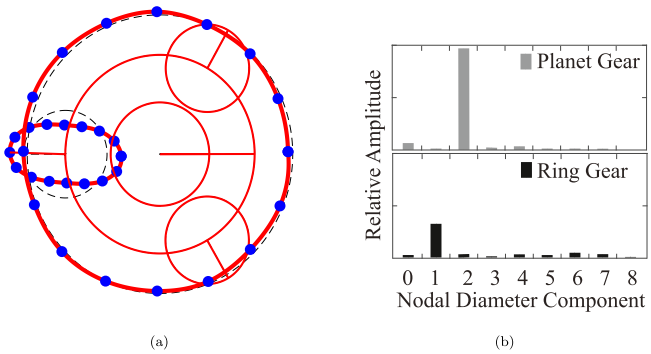

Fig. 26. Planetary gear (a) vibration shape of the fourth dominantly elastic-body mode at 5850 Hz (mode 22) and (b) associated elastic-body nodal diameter components of the ring gear (black bars) and planet gears (gray bars) from FE/CM simulation.

elastic-body mode in Fig. 26 to the first three in Figs. 17 and 19 reveals the qualitative difference between ring-dominant elastic-body modes (numbers 19–21) and the planet-dominant elastic-body mode (number 22).

Similar to the other dominantly elastic-body modes, the 5860 Hz mode contains both discrete-body and elastic-body motion. The mode shape is characterized by the following attributes, given in order of prominence:

- Significant two nodal diameter elastic-body deformation of the planet gears,
- Elastic-body deformation and discrete-body motion of the ring gear,
- Rotational discrete-body motion of the planet gear,
- Increased translational discrete-body motion of the planet gear at higher torque, and
- Carrier translational discrete-body motion at higher torque.

While some elastic-body motion of ring gears is generally expected – especially for thin ring gears – observation of planet elastic-body motion is more surprising, particularly with the bearings in Fig. 8 and a solid shaft inner race (not shown). These planet gears are not intentionally thin or compliant; they are similar in design to production helicopter gears and supported by production helicopter bearings. Planetary gear vibration research and, in our industry interactions, practical design pays little attention to elastic-body vibration of planet gears, but this research reveals that to be a misguided assumption in applications that may achieve higher mesh frequencies that trigger vibration of higher natural frequency modes (e.g., aerospace applications). Planet elastic-body modes may lead to cracks on the planet inner diameter and fatigue failure. At least two catastrophic helicopter crashes resulted from such a failure mode, although it is not established that elastic-body vibration of the planet gears was the root cause [65].

7. Tooth mesh excitation of elastic-body mode vibration

Vibration modes with significant mesh deflection (or mesh strain energy) are of greatest practical concern because they are the most susceptible to excitation from dynamic tooth mesh forces that generally occur at mesh frequency and its harmonics. Here we use FE/CM dynamic simulations and experimental data to demonstrate that the dominantly elastic-body modes are highly susceptible to excitation from dynamic tooth mesh forces.

Numerous independent single-speed FE/CM analyses were conducted at speeds where the mesh frequency coincides with each of the natural frequencies discussed in this paper, including moderately and dominantly elastic-body modes. The steady state dynamic sun-planet and ring-planet mesh forces are calculated through time-domain numerical integration, and the RMS of the fluctuating component of the forces is determined. Fig. 27 shows these mesh forces for each mode. Ring-planet mesh forces in the dominantly elastic-body modes are equal to or greater than those of the moderately elastic-body modes. Note that past research [53] shows that the moderately elastic-body modes, numbers 13–18 and called “gear modes” in the reference, are characterized by high tooth mesh strain energy. Although the highest sun-planet mesh forces occur in the moderately elastic-body modes 17 and 18 (cluster 3), which are known have high mesh deflection [53], the dynamic mesh forces in dominantly elastic-body modes are comparable to those of the moderately elastic-body gear modes. Mesh forces in the elastic ring modes (numbers 19–21) are similar to those in the elastic planet mode (number 22), indicating no meaningful difference in the impact of these two types; both are associated with high mesh deflection.

The high mesh/deflection energy of elastic-body modes is evident experimentally using the driving point accelerometer in Fig. 2b. This sensor is parallel to and close by the ring-planet line of action, so its measurement provides good understanding of vibration present in this mesh. Fig. 28 shows the frequency response plot. Acceleration is provided, consistent with other FRFs in this paper, and so is displacement. These experimental driving-point measurements lead to a similar conclusion as FE/CM simulation: mesh energy in the dominantly elastic-body modes is similar to – and perhaps sometimes greater than – that in the moderately elastic-body modes, which are already known [53] to have significant tooth mesh deflections. These modes are likely to experience high vibration when their natural frequencies are within the operating mesh frequency range.

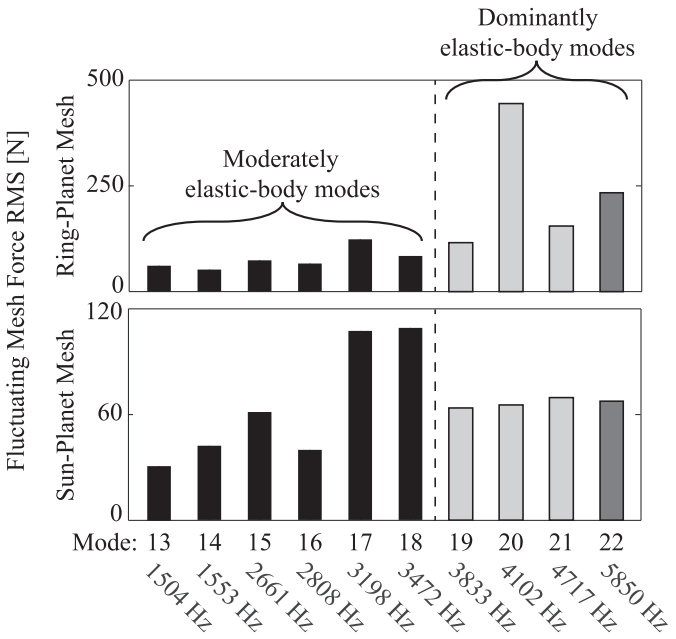

Fig. 27. Fluctuating sun-planet and ring-planet mesh force amplitudes in all moderately and dominantly elastic-body modes from steady-state FE/CM dynamic simulation. Light gray bars are ring dominant modes and the dark gray bar is the planet dominant mode.

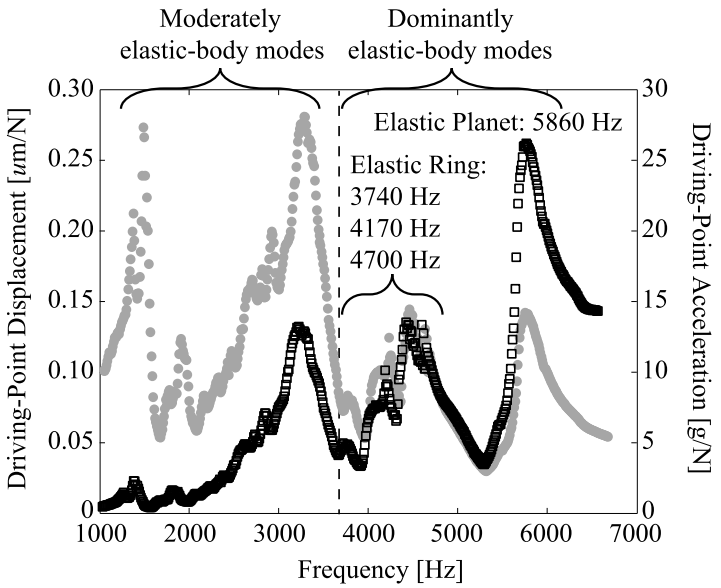

Fig. 28. Shaker testing experimental frequency response of the three-planet system at the driving-point accelerometer in Fig. 2b for displacement (gray solid circles) and acceleration (black open squares).

8. Conclusions

Elastic-body vibration is more common in planetary gears than expected. Ten modes are studied in experiments and verified by finite element/contact mechanics modeling with excellent accuracy on natural frequencies and response amplitudes. This research documents multiple cases of elastic-body vibration in the ring gear and one interesting case with significant elastic-body motion in the planet gears. Experimentally measured nodal diameter components of the ring gear agree with analytical model predictions in the literature based on mode type. The experimental planetary gear has no intentionally designed features to enhance such elastic-body vibration. In fact, it has stiffer, more robust components than used in many practical planetary gears. The ring gear has dimensions close to those of a helicopter planetary gear that has been used for decades. It is attached to a stiff support structure. Nevertheless, elastic-body ring gear vibration occurs. Likewise, no mea-

sures were taken to promote elastic-body motion of the planet gear, yet we see it. More aggressive lightweight designs or those with deliberate elastic-body compliance to promote load sharing or compensate for manufacturing errors can expect elastic-body vibration in even more modes, at greater amplitudes, and at lower frequencies than the present system. If not considered thoroughly, these elastic-body modes can increase noise and stress in unexpected ways in many applications.

Six modes with elastic-body motion were previously predicted by a lumped-parameter model because their elastic-body vibration is moderate compared to the discrete-body vibration, but four dominantly elastic-body modes can not be captured or reasonably approximated by a lumped-parameter model. All are within the frequency range of interest. Each mode couples discrete-body and elastic-body vibration, showing that traditional lumped-parameter models can miss important modal behavior. Measured elastic-body vibration amplitudes are similar to, or greater than, discrete-body vibration amplitudes in many modes. All elastic-body modes considered have high tooth mesh deflections and experience high dynamic mesh forces; mesh excitation sources will strongly excite them. Several cases are shown where elastic-body modes appear in different planet configurations (three, four, and five planets). Dominantly elastic-body modes occur at higher frequencies in the present system, but there is no distinguishing frequency gap between the predominantly discrete-body and elastic-body modes. These mode types will mix and couple even more strongly in more compliant planetary gears, especially aerospace applications. We conclude that all modes likely have at least moderate elastic-body motion, and this is probably the case for many industrial planetary gears.

This work shows the importance of considering elastic-body vibration in planetary gear research and design, especially for the ring gear where elastic-body vibration is prominent in many modes. The measured planet elastic-body vibration is less expected and generally neglected even in models that include elastic-body ring vibration. Such assumptions may need reconsideration, especially in lightweight high-speed applications or systems with intentional compliance to improve load sharing or robustness against manufacturing errors. Elastic/discrete-body coupling with other components, notably the ring gear and carrier, may easily transmit to the surrounding structure. There may be unanticipated resonances situations associated with elastic-body motion causing excess noise, premature wear, fatigue problems (especially at the planet gear inner diameter), or elevated stress on other drivetrain components in many practical gear systems in manufacture and operation today.

Declaration of Competing Interest

The authors declare that they have no known competing financial interests or personal relationships that could have appeared to influence the work reported in this paper.

Acknowledgment

The authors thank Dr. Sandeep Vijayakar of Advanced Numerical Solutions for help with the finite element/contact mechanics modeling and use of the Planetary2D software.

References

[1] H. Ligata, A. Kahraman, An experimental study of the influence of manufacturing errors on the planetary gear stresses and planet load sharing, J. Mech. Des. 130 (4) (2008) 041701.
[2] S. Wang, C. Zhu, C. Song, H. Han, Effects of elastic support on the dynamic behaviors of the wind turbine drive train, Frontiers of Mechanical Engineering 12 (3) (2017) 348–356.
[3] M. Kurushin, V. Balyakin, V. Ossiala, Investigation of the dynamics of gear systems with consideration of a pinion support flexibility, Procedia Eng 176 (2017) 25–36.
[4] C.G. Cooley, R.G. Parker, Vibration of high-speed rotating rings coupled to space-fixed stiffnesses, J Sound Vib 333 (12) (2014) 2631–2648.
[5] F. Jarchow, Development status of epicyclic gears, in: International Power Transmssion and Gearing Conference, ASME, Chicago, 1989, pp. 847–858.
[6] T.A. Stolarski, Analysis of epicyclic gear train with deformable ring, Mech Mach Theory 24 (5) (1989) 363–372.
[7] D. Davies, S. Jenkins, F. Belben, Survey of fatigue failures in helicopter components and some lessons learnt, Eng Fail Anal 32 (2013) 134–151.
[8] A. Hammami, A.F. Del Rincon, F. Chaari, M. Santamaria, F.V. Rueda, M. Haddar, Effects of variable loading conditions on the dynamic behaviour of planetary gear with power recirculation, Measurement 94 (2016) 306–315.
[9] R. August, R. Kasuba, Torsional vibrations and dynamic loads in a basic planetary gear system, Journal of Vibration, Acoustics, Stress, and Reliability in Design 108 (3) (1986) 348–353.
[10] F. Cunliffe, J.D. Smith, D.B. Welbourn, Dynamic tooth loads in epicyclic gears, Journal of Engineering for Industry 95 (2) (1974) 578–584.
[11] A. Kahraman, Load sharing characteristics of planetary transmissions, Mech Mach Theory 29 (8) (1994) 1151–1165.
[12] P. Velex, L. Flamand, Dynamic response of planetary trains to mesh parametric excitations, J. Mech. Des. 118 (1) (1996) 7–14.
[13] J. Lin, R.G. Parker, Analytical characterization of the unique properties of planetary gear free vibration, J Vib Acoust 121 (3) (1999) 316–321.
[14] F. Chaari, M.S. Abbes, F. Viadero Rueda, F. del Rincon, M. Haddar, Analysis of planetary gear transmission in non-stationary operations, Frontiers of Mechanical Engineering 8 (1) (2013) 88–94.
[15] F.S. Aski, M. Mirparizi, F.S. Samani, M.A. Hajabasi, Vibration behavior optimization of planetary gear sets, Propul. Power Res. 3 (4) (2014) 196–206.
[16] R. Chen, J. Zhou, W. Sun, Dynamic characteristics of a planetary gear system based on contact status of the tooth surface, J. Mech. Sci. Technol. 32 (1) (2018) 69–80, doi:10.1007/s12206-017-1208-8.
[17] A. Kahraman, Natural modes of planetary gear trains, J Sound Vib 173 (1) (1994) 125–130, doi:10.1006/jsvi.1994.1222.
[18] A. Kahraman, Planetary gear train dynamics, J. Mech. Des. 116 (3) (1993) 713–720.
[19] A. Saada, P. Velex, An extended model for the analysis of the dynamic behavior of planetary trains, J. Mech. Des. 117 (2) (1995) 241–247.
[20] T. Eritenel, R.G. Parker, Modal properties of three-dimensional helical planetary gears, J Sound Vib 325 (1–2) (2009) 397–420, doi:10.1016/j.jsv.2009.03.002.
[21] S. Huang, W. Soedel, Effects of coriolis acceleration on the free and forced in-plane vibrations of rotating rings on elastic foundation, J Sound Vib 115 (2) (1987) 253–274.

[22] J. Lin, W. Soedel, On general in-plane vibrations of rotating thick and thin rings, May 3122 (3) (1988) 547–570.
[23] T. Charnley, R. Perrin, V. Mohanan, H. Banu, Vibrations of thin rings of rectangular cross-section, J Sound Vib 138 (3) (1989) 455–488.
[24] W. Kim, J. Chung, Free non-linear vibration of a rotating thin ring with the in-plane and out-of-plane motions, J Sound Vib 258 (1) (2002) 167–178.
[25] A. Kahraman, S.M. Vijayakar, Effect of internal gear flexibility on the quasi-static behavior of a planetary gear set, J. Mech. Des. 123 (3) (2001) 408–415.
[26] A. Kahraman, A.A. Kharazi, M. Umrani, A deformable body dynamic analysis of planetary gears with thin rims, J Sound Vib 262 (3) (2003) 752–768.
[27] N. Ge, J. Zhang, Finite element analysis of internal gear in high-speed planetary gear units, Transactions of Tianjin University 14 (1) (2008) 1115.
[28] V. Abousleiman, P. Velex, A hybrid 3d finite element/lumped parameter model for quasi-static and dynamic analyses of planetary/epicyclic gear sets, Mech Mach Theory 41 (6) (2006) 725–748.
[29] V. Abousleiman, P. Velex, S. Becquerelle, Modeling of spur and helical gear planetary drives with flexible ring gears and planet carriers, J. Mech. Des. 129 (2007) 95–106, doi:10.1115/1.2359468.
[30] M. Chapron, P. Velix, J. Bruyere, S. Becquerelle, Optimization of profile modifications with regard to dynamic tooth loads in single and double-helical planetary gears with flexible ring-gears, J. Mech. Des. 138 (2) (2016) 023301.
[31] J. Zhang, Y. Song, J. Xu, A discrete lumped-parameter dynamic model for a planetary gear set with flexible ring gear, Applied Mechanics and Materials 86 (2011) 756–761.
[32] J. Wei, A. Zhang, D. Qin, T.C. Lim, R. Shu, X. Lin, F. Meng, A coupling dynamics analysis method for a multistage planetary gear system, Mech Mach Theory 110 (2017) 27–49.
[33] A. Zhang, J. Wei, D. Qin, S. Hou, Analytical coupling characterization of multi-stage planetary gear free vibration considering flexible structure, Journal of Vibroengineering 16 (6) (2017) 2583.
[34] Z. Zeng, K. Ding, G. He, W. Li, Space-time model and spectrum mechanism on vibration signal for planetary gear drive, Mech Syst Signal Process 129 (2019) 164–185.
[35] C. Zhang, J. Wei, W. Wang, S. Hou, A. Zhang, T. Lim, Dynamic model and load sharing performance of planetary gear system with journal bearing, Mech Mach Theory 151 (2020) 103898.
[36] R.P. Tanna, T.C. Lim, Modal frequency deviations in estimating ring gear modes using smooth ring solutions, J Sound Vib 269 (3–5) (2004) 1099–1110.
[37] X. Wu, R.G. Parker, Modal properties of planetary gears with an elastic continuum ring gear, J Appl Mech 75 (3) (2008) 1–10.
[38] R.G. Parker, X. Wu, Vibration modes of planetary gears with unequally spaced planets and an elastic ring gear, J Sound Vib 329 (11) (2010) 2265–2275, doi:10.1016/j.jsv.2009.12.023.
[39] R.G. Parker, X. Wu, Parametric instability of planetary gears having elastic continuum ring gears, J Vib Acoust 134 (4) (2012) 041011, doi:10.1115/1.4005836.
[40] C. Wang, R.G. Parker, Dynamic modeling and mesh phasing-based spectral analysis of quasi-static deformations of spinning planetary gears with a deformable ring, Mech Syst Signal Process 136 (2020) 106497, doi:10.1016/j.ymssp.2019.106497.
[41] S. Wang, M. Huo, C. Zhang, J. Liu, Y. Song, S. Cao, Y. Yang, Effect of mesh phase on wave vibration of spur planetary ring gear, Eur. J. Mech. A. Solids 30 (6) (2011) 820–827, doi:10.1016/j.euromechsol.2011.06.004.
[42] Z. Chen, Y. Shao, Mesh stiffness of an internal spur gear pair with ring gear rim deformation, Mech Mach Theory 69 (2013) 1–12.
[43] Z. Chen, Y. Shao, D. Su, Dynamic simulation of planetary gear set with flexible spur ring gear, J Sound Vib 332 (26) (2013) 7191–7204.
[44] Z. Chen, Z. Zhu, Y. Shao, Fault feature analysis of planetary gear system with tooth root crack and flexible ring gear rim, Eng Fail Anal 49 (2015) 92–103.
[45] T. Hidaka, Y. Terauchi, K. Ishioka, Dynamic behavior of planetary gear (2nd report, displacement of sun gear and ring gear), Bulletin of the JSME 19 (138) (1976) 1563–1570.
[46] T. Hidaka, Y. Terauchi, M. Nohara, J. Oshita, Dynamic behavior of planetary gear (3rd report, displacement of ring gear in direction of line of action), Bulletin of the JSME 20 (150) (1977) 1663–1672.
[47] X. Wu, R.G. Parker, Vibration of rings on a general elastic foundation, J Sound Vib 295 (1–2) (2006) 194–213.
[48] S. Oda, M. Miyachika, Root stress of thin-rimmed internal spur gear supported with pins, JSME International Journal 30 (262) (1987) 646–652.
[49] T. Hidaka, Y. Terauchi, K. Nagamura, Dynamic behavior of planetary gear (7th report, influence of the thickness of the ring gear), Bulletin of the JSME 22 (170) (1979) 1142–1149.
[50] A. Kahraman, H. Ligata, A. Singh, Influence of ring gear rim thickness on planetary gear set behavior, J. Mech. Des. 132 (2) (2010) 021002, doi:10.1115/1.4000699.
[51] C. Vicuña, F. Chaari, Analysis of a Planetary Gearbox Under Non-stationary Operating Conditions: Numerical and Experimental Results, Springer International, pp. 351–362. 10.1007/978-3-319-20463-5_26
[52] A. Mbarek, A. Fernández Del Rincon, A. Hammami, M. Iglesias, F. Chaari, F. Viadero, M. Haddar, Comparison of experimental and operational modal analysis on a back to back planetary gear, Mech Mach Theory 124 (2018) 226–247.
[53] T.M. Ericson, R.G. Parker, Planetary gear modal vibration experiments and correlation against lumped-parameter and finite element models, J Sound Vib 332 (9) (2013) 2350–2375, doi:10.1016/j.jsv.2012.11.004.
[54] T.M. Ericson, R.G. Parker, Experimental measurement of the effects of torque on the dynamic behavior and system parameters of planetary gears, Mech Mach Theory 74 (2014) 370–389.
[55] C.G. Cooley, R.G. Parker, Limitations of an inextensible model for the vibration of high-speed rotating elastic rings with attached space-fixed discrete stiffnesses, Eur. J. Mech. A. Solids 54 (2015) 187–197.
[56] P. Ma, M. Botman, Load sharing in a planetary gear stage in the presence of errors and misalignment, Journal of Mechanisms, Transmissions, and Automation in Design - Transactions of the ASME 107 (Sp. Iss.) (1985) 4–10.
[57] J. McNames, Fourier series analysis of epicyclic gearbox vibration, J Vib Acoust 124 (1) (2002) 150–153.
[58] S.M. Vijayakar, A combined surface integral and finite-element solution for a three-dimensional contact problem, Int J Numer Methods Eng 31 (3) (1991) 525–545.
[59] S.M. Vijayakar, Planetary2D User's Manual, Advanced Numerical Solutions LLC, Hilliard, Ohio, 43026 USA, 2006.
[60] R.G. Parker, S.M. Vijayakar, T. Imajo, Non-linear dynamic response of a spur gear pair: modelling and experimental comparisons, J Sound Vib 237 (3) (2000) 435–455.
[61] A. Singh, A. Kahraman, H. Ligata, Internal gear strains and load sharing in planetary transmissions: model and experiments, J. Mech. Des. 130 (7) (2008) 072602, doi:10.1115/1.2890110.
[62] H. Ligata, A. Kahraman, A. Singh, A closed-form planet load sharing formulation for planetary gear sets using a translational analogy, J. Mech. Des. 131 (2) (2009) 021007.
[63] S. Schweiki, A. Rezayat, T. Tamarozzi, D. Mundo, Transmission error and strain analysis of lightweight gears by using a hybrid fe-analytical gear contact model, Mech Syst Signal Process 123 (2019) 573–590.
[64] T.M. Ericson, R.G. Parker, Natural frequency clusters in planetary gear vibration, J Vib Acoust 135 (6) (2013) 061002.
[65] Accident Investigation Board Norway, "Summary Report on the Air Accident Near Turnøy, Norway 29 April 2016 with Airbus Helicopters EC 225 LP, LN-OJF", Technical Report, Aibn, 2018.